Surface & Coatings Technology 401 (2020) 126237

Contents lists available at ScienceDirect

Surface & Coatings Technology

journal homepage: www.elsevier.com/locate/surfcoat

Self-organized columnar $Zr_{0.7}Ta_{0.3}B_{1.5}$ core/shell-nanostructure thin films

Babak Bakhit[a,*], Justinas Palisaitis[a], Per O.Å. Persson[a], Björn Alling[b], Johanna Rosen[a], Lars Hultman[a], Ivan Petrov[a,c,d], J.E. Greene[a,c,d], Grzegorz Greczynski[a]

[a] Thin Film Physics Division, Department of Physics (IFM), Linköping University, Linköping SE-58183, Sweden
[b] Theoretical Physics, Department of Physics (IFM), Linköping University, Linköping SE-58183, Sweden
[c] Materials Research Laboratory and Department of Materials Science, University of Illinois, Urbana IL 61801, USA
[d] Department of Materials Science and Engineering, National Taiwan University of Science and Technology, Taipei 10607, Taiwan

ARTICLE INFO

Keywords:
Thin films
Transition-metal (TM) diborides
Self-organized
Core/shell nanostructure
Hardness and toughness

ABSTRACT

We recently showed that $Zr_{1-x}Ta_xB_y$ thin films have columnar nanostructure in which column boundaries are B-rich for $x < 0.2$, while Ta-rich for $x \geq 0.2$. Layers with $x \geq 0.2$ exhibit higher hardness and, simultaneously, enhanced toughness. Here, we determine the atomic-scale nanostructure of sputter-deposited columnar $Zr_{0.7}Ta_{0.3}B_{1.5}$ thin films. The columns, 95 ± 17 Å, are core/shell nanostructures in which 80 ± 15-Å cores are crystalline hexagonal-AlB_2-structure Zr-rich stoichiometric $Zr_{1-x}Ta_xB_2$. The shell structure is a narrow dense, disordered region that is Ta-rich and highly B-deficient. The cores are formed under intense ion mixing via preferential Ta segregation, due to the lower formation enthalpy of TaB_2 than ZrB_2, in response to the chemical driving force to form a stoichiometric compound. The films with unique combination of nanosized crystalline cores and dense metallic-glass-like shells provide excellent mechanical properties.

1. Introduction

Refractory transition-metal (TM) diborides, classified as ultra-high temperature ceramics, are of increasing interest for use as hard ceramics in many applications, particularly in extreme environments [1–3], such as hypersonic aerospace vehicles and rockets [2–8], nuclear reactors [9–11], solar power [12–15], optoelectronic and microelectronic components [16–18], and cutting tools [19–22]. This broad range of applications is due to the unique combination of properties including high melting point [23,24], high hardness and incompressibility [25–34], good corrosion resistance [35,36], metal-like electrical conductivity [37–43], high thermal and chemical stability [38,44,45], electrocatalytic features [46–48], and ferromagnetism [49]. TM diboride thin films crystallize in the hexagonal AlB_2 crystal structure (P6/mmm, SG-191), in which densely packed metal atom layers are held on atop positions (with respect to the neighboring metal layers) by graphite-like sheets of boron atoms [50]. The diffusivity of boron, which is higher than TM elements [51,52], largely depends on the composition and deposition temperature [53]. Boron atoms show anisotropic transport in the hexagonal AlB_2 structure [52,53] with a preferred diffusion path between the (0001) basal planes [53]. As opposed to TM nitrides, which have very wide single-phase compound fields [54,55], TM diborides are line compounds [23,56]. This can cause serious challenges for sputter depositing stoichiometric diboride layers, with B-to-metal ratio of 2 [57,58].

While most hard ceramics are brittle [59], we have demonstrated that $Zr_{1-x}Ta_xB_y$ thin films with $x \geq 0.2$ are not only hard, but also tough [60]. The alloys were grown in pure Ar by hybrid high-power impulse and dc magnetron (HiPIMS and DCMS) co-sputtering [61–63] in which a compound ZrB_2 target was continuously sputtered by DCMS, while a Ta target was operated in HiPIMS mode. A negative substrate bias was applied in synchronous with the metal-ion-rich portion of each HiPIMS pulse; at all other times, the substrate was electrically floating. Layers grown by pure DCMS were found to be overstoichiometric with composition $ZrB_{2.4}$. The B-to-metal ratio $y = B/(Zr + Ta)$ in $Zr_{1-x}Ta_xB_y$ alloy films decreased continuously, while the Ta-cation ratio $x = Ta/(Zr + Ta)$ increased, with increasing power applied to the HiPIMS Ta target.

A combination of x-ray diffraction, transmission electron microscopy (TEM), energy-dispersive x-ray spectroscopy (EDX), electron energy-loss spectroscopy, and atom-probe tomography (APT) revealed that all films have the hexagonal AlB_2 crystal structure with a columnar nanostructure, in which the column boundaries of layers with $x < 0.2$ are B-rich, whereas those with $x \geq 0.2$ are Ta-rich. The nanocolumn structure, combined with changes in average column widths, resulted in $Zr_{0.7}Ta_{0.3}B_{1.5}$ layers exhibiting an ~20% increase in hardness, from 35

* Corresponding author.
E-mail address: babak.bakhit@liu.se (B. Bakhit).

https://doi.org/10.1016/j.surfcoat.2020.126237
Received 1 July 2020; Accepted 26 July 2020
Available online 27 July 2020

to 42 GPa, with a simultaneous increase of ~30% in nanoindentation toughness, from 4.0 to 5.2 MPa√m, compared to $ZrB_{2.4}$ [60]. Here, we focus on the $Zr_{0.7}Ta_{0.3}B_{1.5}$ layers, which have both high hardness as well as the highest toughness, to determine their detailed atomic-scale nanostructure.

2. Experimental

The films, 1.6-μm thick, are deposited on 1.5 × 1.5 cm^2 Si(001) substrates at 475 °C in a CC800/9 CemeCon AG sputtering system with a base pressure of 3.8 × 10^{-6} Torr (0.5 mPa) using hybrid Ta-HiPIMS/ZrB_2-DCMS co-sputtering. The ZrB_2 DCMS target is continuously sputtered at 5 kW, while the Ta magnetron is operated in HiPIMS mode, with 50-μs HiPIMS pulses, at an average power of 1800 W and a frequency of 300 Hz to provide a pulsed source of energetic Ta ions [60]. A 100-V negative bias is applied to the substrate in synchronous with the metal-ion-rich portion of each HiPIMS pulse, as determined by time-resolved mass spectroscopy analyses at the substrate position [64,65], starting from t = 30 μs following pulse initiation (t = 0) to t = 130 μs. At all other times, the substrate is at a negative floating potential of 10 V. The target-to-substrate separation is 20 cm, yielding a deposition rate of ~10 Å/s (3.6 μm/h). Time- and energy-resolved mass spectroscopy measurements show that the $Ta^{2+}/(Ta^{+} + Ta^{2+})$ ratio incident at the substrate during each 100-μs synchronized substrate bias pulse is 0.052; additional details are given in reference 60.

Average film compositions are determined by time-of-flight elastic-recoil detection analyses in a tandem accelerator with a 36 MeV $^{127}I^{8+}$ probe beam incident at 67.5° with respect to the sample surface normal; recoils are detected at 45°. High-resolution plan-view TEM analyses are carried out in a monochromated and aberration-corrected FEI Titan^3 60–300 electron microscope operated at 300 kV; high-angle annular dark-field (HAADF) images are acquired in scanning TEM (STEM) mode, using a 145-mm camera length, with the inner and outer acceptance HAADF-detector angles ranging from 56 to 200 mrad. EDX elemental maps are obtained using the SuperX and GIF Quantum ERS spectrometers embedded in the FEI instrument. Plan-view TEM specimens are prepared by mechanically polishing the samples from the substrate side, followed by Ar^{+} ion milling at 5 keV, with a 6° incidence angle, during sample rotation in a Gatan precision ion miller. For the final stages of sample thinning, the ion energy is reduced to 2.5 keV.

3. Results and discussion

Typical plan-view bright-field (BF) TEM, dark-field (DF) TEM, and HAADF-STEM images of $Zr_{0.7}Ta_{0.3}B_{1.5}$ films are shown in Fig. 1. The inset in Fig. 1(a) presents a cross-sectional BF-TEM image, with the corresponding selected-area electron diffraction (SAED) pattern, showing that the films are highly oriented with a [0001] fiber texture and consist of nanocolumns which extend in the growth direction. The plan-view images are acquired normal to the [0001] fiber texture axis. The plan-view BF-TEM image, Fig. 1(a), reveals that the nanocolumns have an average size of 95 ± 17 Å, with a contrast difference between lighter column cores and darker shell regions. The plan-view DF-TEM image in Fig. 1(b) exhibits dark cores surrounded by bright shells. Individual columns that are perfectly aligned with their [0001] zone axis, normal to the beam, appear dark in the BF-TEM image, while they are bright in the DF-TEM image, as indicated by arrows in Fig. 1(a) and (b). In both images, the difference in intensities between columns originates from differences in beam scattering and absorption conditions between individual columns. The plan-view SAED pattern in the Fig. 1(b) inset is characterized by a dominant [$10\bar{1}0$] reflection, which is in agreement with the strong [0001] fiber texture of the film in the growth direction. A change in contrast between the core and shell regions is also observed in the plan-view mass-sensitive (HAADF-STEM) image, Fig. 1(c), where the brighter shells correspond to enrichment in high-Z Ta. In addition, the enhanced brightness observed for some columns in Fig. 1(c), exemplified by an arrow, originates from well aligned columns that provide conditions for the electron channeling of the convergent beam. The contrast differences between cores and shells in all three images are attributed to differences in composition and/or structure.

High-resolution plan-view HAADF-STEM images of $Zr_{0.7}Ta_{0.3}B_{1.5}$ films acquired along the [0001] zone axis, as well as off axis, are shown in Fig. 2. The plan-view zone-axis HAADF-STEM image, Fig. 2(a), for which the electron-channeling conditions are optimized, reveals that contrast within individual diboride crystalline cores is relatively homogeneous, while the shell regions are darker. We attribute the distinct contrast change to the presence of a disordered, primarily metal, shell phase surrounding each crystalline core. The slightly tilted plan-view image in Fig. 2(b), where the electron-channeling effects are strongly reduced and Z-contrast is dominant, reveals brighter shell regions. This indicates, in agreement with the above results, that the shell regions have a larger concentration of higher-mass Ta (m_{Ta} = 180.9 amu vs. m_{Zr} = 91.2 amu, and m_B = 10.8 amu), which segregates toward boundaries with corresponding Zr-rich central core region.

A high-resolution plan-view HAADF-STEM image, Fig. 2(c), obtained along the [0001] zone axis, shows that the core regions are crystalline with a hexagonal structure, while the Ta-rich shells are

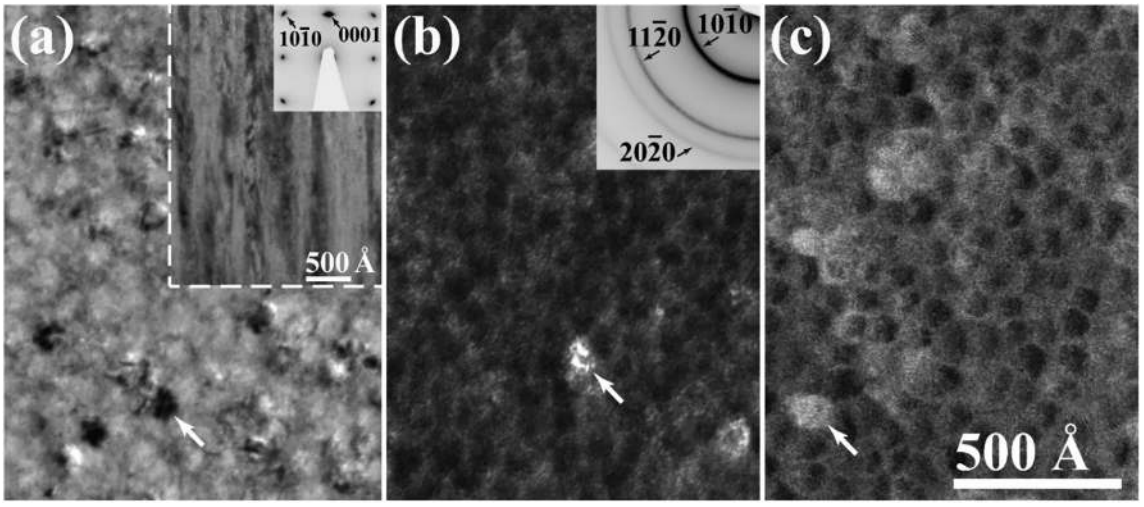

Fig. 1. Plan-view (a) bright-field TEM image, with cross-sectional bright-field TEM image and the corresponding SAED pattern shown in the inset; (b) dark-field TEM image together with the corresponding SAED pattern; and (c) HAADF-STEM image of $Zr_{0.7}Ta_{0.3}B_{1.5}$ films.

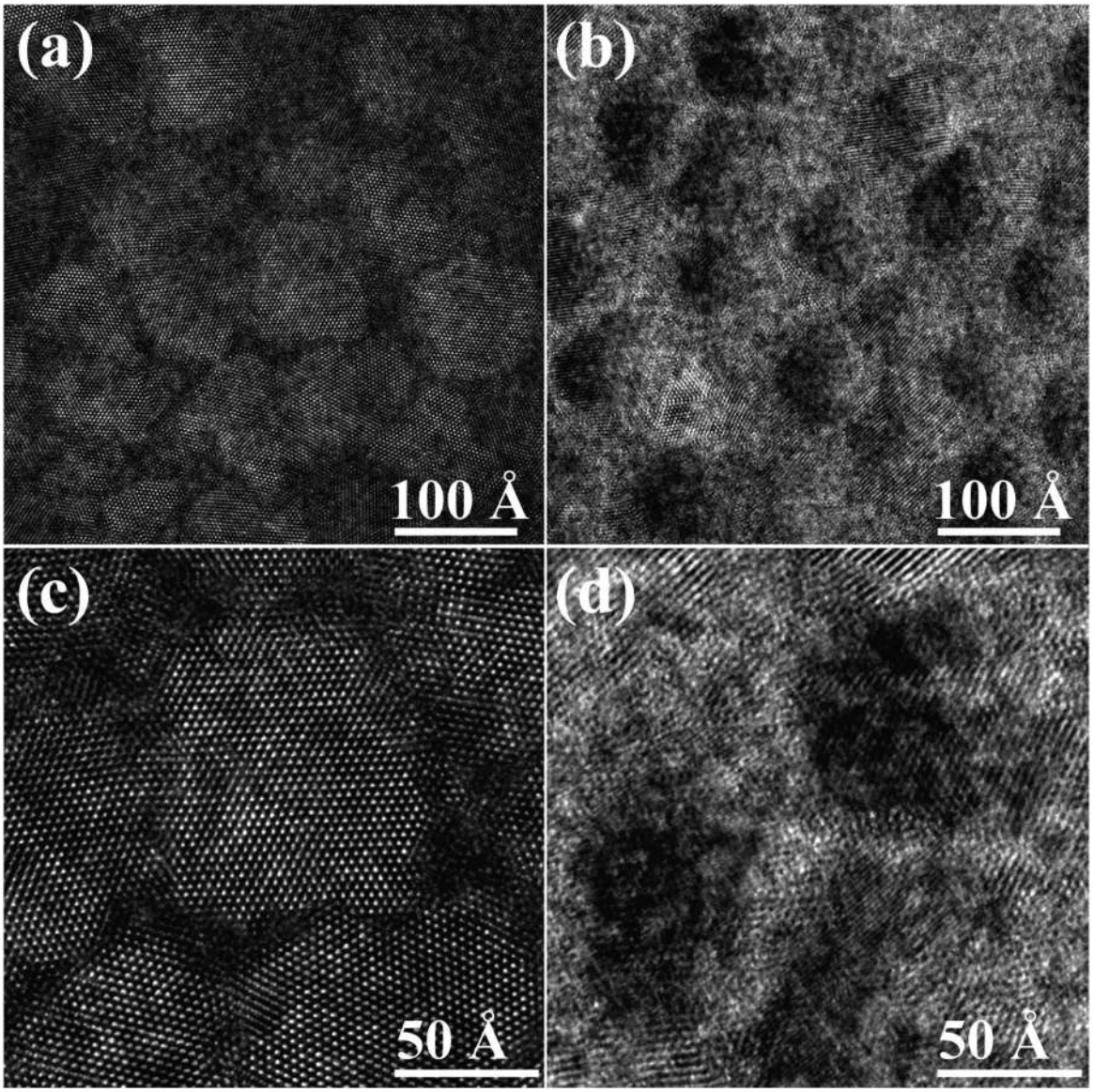

Fig. 2. High-resolution plan-view HAADF-STEM images acquired: (a) and (c) along the [0001] zone axis and (b) and (d) off zone axis from $Zr_{0.7}Ta_{0.3}B_{1.5}$ films.

disordered and similar to metallic glasses [66–68]. This is shown more clearly in Fig. 2(d), a higher-resolution plan-view off-zone-axis image acquired from the same sample region as Fig. 2(b). Since the electron-channeling condition is minimized in this image, the variation in contrast is due to brighter Ta-rich compositional modulations. The average width, estimated from the zone-axis images, of the crystalline core regions is 80 ± 15 Å, while the disordered shell regions are 15 ± 8 Å wide.

The Ta-rich shell regions appear significantly wider in the off-zone-axis images, Fig. 2(b) and (d), than in the zone-axis images, Fig. 2(a) and (c). This is due to the projection of the tilted columnar structure with resulting overlay contrast from cores and shells.

Fig. 3 shows the high-resolution cross-sectional HAADF-STEM image of $Zr_{0.7}Ta_{0.3}B_{1.5}$, which exhibits the shell structure between two adjacent cores, and confirms that the cores are crystalline, while the shells are disordered regions. In addition, it clearly reveals the collapse of diboride layered structure in the cores into a disordered shell.

In order to probe Zr and Ta elemental distributions in the $Zr_{0.7}Ta_{0.3}B_{1.5}$ core/shell nanostructures, plan-view EDX maps are acquired from the same sample region as the off-zone-axis image in Fig. 2(b). The Zr EDX map, shown in red in Fig. 4(a), reveals a relatively uniform distribution of Zr. The contrast variations in the Ta EDX map, Fig. 4(b), are locally much more pronounced. This is seen more clearly in the combined Zr and Ta EDX map in Fig. 4(c), which reveals that the amount of Ta in the disordered shell boundaries is higher than in the crystalline cores, consistent with previous APT results [60].

A schematic plan-view illustration of $Zr_{0.7}Ta_{0.3}B_{1.5}$ films grown using the hybrid Ta-HiPIMS/ZrB_2-DCMS co-sputtering is shown in Fig. 5. ZrB_2 forms a solid solution with TaB_2, both of which have the AlB_2 hexagonal crystal structure [24,69], in the central core regions. The ZrB_2/TaB_2 lattice mismatch along the *a* direction is 2.2% (a_{ZrB2} = 3.169 Å and a_{TaB2} = 3.098 Å [70,71]), while the mismatch along the *c* direction is much larger, 8.6% (c_{ZrB2} = 3.530 Å and c_{TaB2} = 3.227 Å [70,71]), which provides lattice buckling and a driving force for phase separation during film deposition where adatom diffusivity is active and atomic layers can partly relax upwards (bulk diffusion quenched). The TM diborides are line compounds [23,56], for which TaB_2 has a much lower formation enthalpy (−2.16 eV/atom) [72,73] than ZrB_2 (−3.35 eV/atom) [72,73]. Thus, the overall understoichiometry of the present $Zr_{0.7}Ta_{0.3}B_{1.5}$ alloys results in Ta segregation, during film growth, toward the shell regions in order to maintain the central core regions stoichiometric.

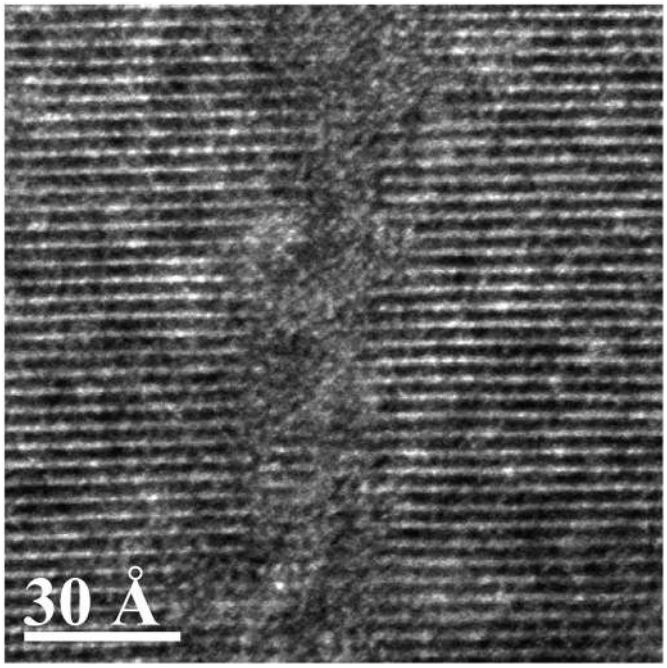

Fig. 3. High-resolution cross-sectional HAADF-STEM image of $Zr_{0.7}Ta_{0.3}B_{1.5}$ films.

This gives rise to a change in the cation fraction from Zr-rich central core regions to higher Ta concentrations in the shells, consistent with density-functional-theory calculations of Dahlqvist et al. [74] showing that TaB_2 is more tolerant than ZrB_2 to the formation of B vacancies. The understoichiometric Ta-rich/B-deficient shells are disordered due to the collapse of the hexagonal planes, confirmed in Fig. 3, as the B vacancy concentration becomes too high to sustain the AlB_2 structure in which TM atoms reside above hexagonal B interstices.

There is an increase of ~30% in the metal-atom volume density due to a transition from AlB_2 structure, in which the metal atoms are held in atop positions with respect to the neighboring metal atomic layer by B atoms arranged in hexagonal rings, to a disordered structure in which the metal atoms are more closely packed. The disordered shell has the structural characteristics of metallic-glass thin films, which have been shown to exhibit both high strength and toughness [66–68].

4. Conclusions

$Zr_{0.7}Ta_{0.3}B_{1.5}$ alloy films, grown at 475 °C by hybrid high-power impulse (HiPIMS) and dc magnetron (DCMS) co-sputtering, in which a ZrB_2 target is continuously sputtered by DCMS and a Ta target is operated in HiPIMS mode, have a highly oriented [0001] fiber texture. They are both hard and ductile as reported in reference 60. Here, a combination of high-resolution TEM, HAADF-STEM, and EDX analyses is used to determine the atomic-scale nanostructure of $Zr_{0.7}Ta_{0.3}B_{1.5}$ alloys, which is responsible for their excellent mechanical properties. The columns, with average diameters of 95 ± 17 Å, are core/shell nanostructures in which the 80 ± 15-Å cores are crystalline Zr-rich B-stoichiometric $Zr_{1-x}Ta_xB_2$. The shell structure between adjacent cores is a narrow dense, disordered region which is Ta-rich and highly B-deficient. The cores are formed under intense ion mixing via preferential Ta segregation, due to the lower formation enthalpy of TaB_2 than ZrB_2 (which are both line compounds), in response to the chemical driving force to form a stoichiometric compound. Such a self-organized core/shell nanostructure combines the benefits of crystalline diboride nanocolumns, providing the high hardness, with the dense metallic-glass-like shells, which gives rise to enhanced toughness.

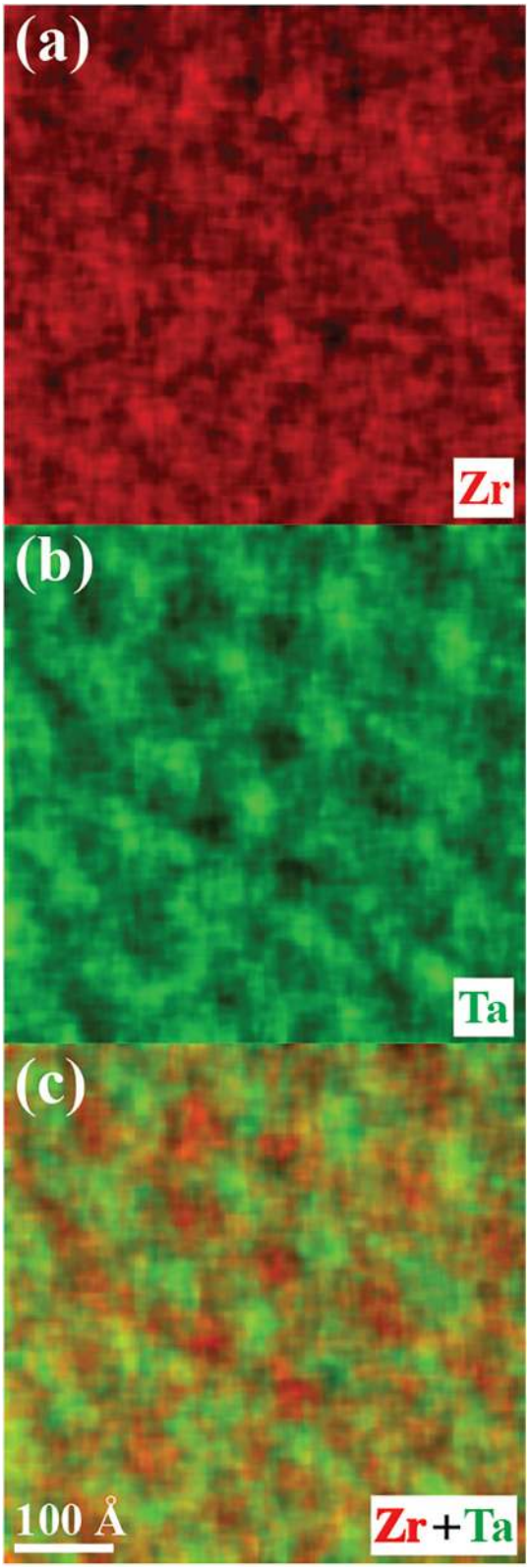

Fig. 4. Plan-view (a) Zr, (b) Ta, and (c) (Zr + Ta) EDX elemental maps obtained from the same area as the off-zone-axis $Zr_{0.7}Ta_{0.3}B_{1.5}$ image in Fig. 2(b).

Declaration of competing interest

The authors declare that they have no known competing financial interests or personal relationships that could have appeared to

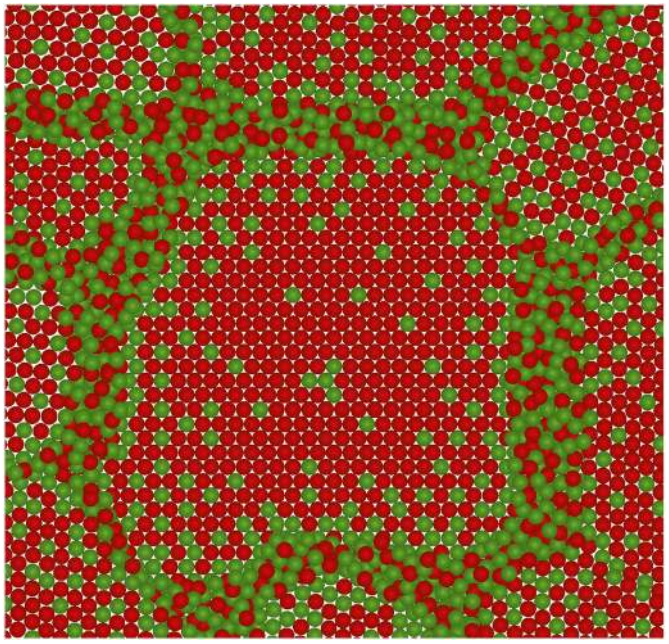

Fig. 5. Schematic plan-view illustration of TM cation distributions in $Zr_{0.7}Ta_{0.3}B_{1.5}$ films with self-organized crystalline Zr-rich $ZrTaB_2$ cores surrounded by disordered Ta-rich/B-deficient shells. Zr atoms are shown in red, while Ta atoms are green (B atoms are not shown). (For interpretation of the references to color in this figure legend, the reader is referred to the web version of this article.)

influence the work reported in this paper.

Acknowledgements

The authors gratefully acknowledge Professor Jian-Min Zuo from University of Illinois for useful discussions. We acknowledge support from the Knut and Alice Wallenberg (KAW) Foundation for Project funding (KAW 2015.0043), a Fellowship/Scholar Grant, and support of the electron microscopy laboratory in Linköping. Financial support from the Swedish Research Council VR Grant 2014-5790, 2018-03957, 2019-05403, and 642-2013-8020, the VINNOVA Grant 2018-04290, an Åforsk Foundation grant #16-359, and Carl Tryggers Stiftelse contracts CTS 15:219, CTS 17:166, and CTS 14:431 is also gratefully acknowledged. Furthermore, the authors acknowledge financial support from the Swedish Government Strategic Research Area in Materials Science on Functional Materials at Linköping University (Faculty Grant SFO Mat LiU No. 2009 00971). Support from the Swedish Research Council VR-RFI (#2017-00646_9) for the Accelerator based ion-technological center and from the Swedish Foundation for Strategic Research for the tandem accelerator laboratory in Uppsala University (contract RIF14-0053) and for Strategic Research through the Future Research Leaders 6 program (contract FFL 15-0290) is acknowledged.

References

[1] E. Wuchina, E. Opila, M. Opeka, W. Fahrenholtz, I. Talmy, UHTCs: Ultra-High Temperature Ceramic materials for extreme environment applications, Electrochem. Soc. Interf. 16 (2007) 30–36.
[2] W.G. Fahrenholtz, E.J. Wuchina, W.E. Lee, Y. Zhou, Ultra-high Temperature Ceramics: Materials for Extreme Environment Applications, First ed., Wiley, Hoboken, NJ, 2014.
[3] W.G. Fahrenholtz, G.E. Hilmas, Ultra-high temperature ceramics: materials for extreme environments, Scripta Mater 129 (2017) 94–99.
[4] J.D. Kellner, W.J. Croft, L.A. Shepard, Titanium Diboride Electrodeposited Coatings, Defense Technical Information Center, ADA047956, (1997).
[5] K. Upadhya, J. Yang, W. Hoffman, Advanced materials for ultrahigh temperature structural applications above 2000 °C, Am. Ceram. Soc. Bull. 76 (1997) 51–56.
[6] J.C. Zhao, J.H. Westbrook, Ultrahigh-temperature materials for jet engines, MRS Bull. 28 (2003) 622–630.
[7] M. Tului, G. Marino, T. Valente, Plasma spray deposition of ultra high temperature ceramics, Surf. Coat. Technol. 201 (2006) 2103–2108.
[8] F. Monteverde, L. Scatteia, Resistance to thermal shock and to oxidation of metal diborides-SiC ceramics for aerospace application, J. Am. Ceram. Soc. 90 (2007) 1130–1138.
[9] B.L. Doyle, W.R. Wampler, D.K. Brice, S.T. Picraux, Saturation and isotopic replacement of deuterium in low-z materials, J. Nucl. Mater. 93-94 (1980) 551–557.
[10] T. Shikama, T. Noda, M. Fukutomi, M. Okada, Deuterium retention in $Ti_{1-x}B_x$ films deposited onto molybdenum by co-sputtering method, J. Nucl. Mater. 141-143 (1986) 156–159.
[11] C.G. Windsor, J.M. Marshall, J.G. Morgan, J. Fair, G.D.W. Smith, A. Rajczyk-Wryk, J.M. Tarragó, Design of cemented tungsten carbide and boride-containing shields for a fusion power plant, Nucl. Fusion 58 (2018) 076014–076026.
[12] E. Sani, L. Mercatelli, D. Jafrancesco, J.L. Sans, D. Sciti, Ultra-high temperature ceramics for solar receivers: spectral and high-temperature emittance characterization, J Eur. Opt. Soc. Rap. Public. 7 (2012) 12052.
[13] L. Mercatelli, E. Sani, D. Jafrancesco, P. Sansoni, D. Fontani, M. Meucci, S. Coraggia, L. Marconi, J.L. Sans, E. Beche, L. Silvestroni, D. Sciti, Ultra-refractory diboride ceramics for solar plant receivers, Energy Proced 49 (2014) 468–477.
[14] E. Sani, M. Meucci, L. Mercatelli, D. Jafrancesco, J.L. Sans, L. Silvestroni, D. Sciti, Optical properties of boride ultrahigh-temperature ceramics for solar thermal absorbers, J Photon. Energy 4 (2014) 045599.
[15] E. Sani, M. Meucci, L. Mercatelli, A. Balbo, C. Musa, R. Licheri, R. Orrù, G. Cao, Titanium diboride ceramics for solar thermal absorbers, Sol. Energy Mater. Sol. Cells 169 (2017) 313–319.
[16] G. Sade, J. Pelleg, Co-sputtered TiB_2 as a diffusion barrier for advanced microelectronics with Cu metallization, Appl. Surf. Sci. 91 (1) (1995) 263–268.
[17] J. Suda, H. Matsunami, Heteroepitaxial growth of group-III nitrides on lattice-matched metal boride ZrB_2 (0001) by molecular beam epitaxy, J. Cryst. Growth 237-239 (2002) 1114–1117.
[18] J. Sung, D.M. Goedde, G.S. Girolami, J.R. Abelson, Remote-plasma chemical vapor deposition of conformal ZrB_2 films at low temperature: a promising diffusion barrier for ultralarge scale integrated electronics, J. Appl. Phys. 91 (2002) 3904–3911.
[19] Babak Bakhit, Justinas Palisaitis, Jimmy Thörnberg, Johanna Rosen, Per O.Å. Persson, Lars Hultman, Ivan Petrov, J.E. Greene, Grzegorz Greczynski, Improving the high-temperature oxidation resistance of TiB_2 thin films by alloying with Al, Acta Materialia 196 (2020) 677–689, https://doi.org/10.1016/j.actamat.2020.07.025.
[20] A.A. Goncharov, S.N. Dub, A.V. Agulov, V.V. Petukhov, Structure, composition, and mechanical properties of thin films of transition metals diborides, J Superhard Mater 37 (2015) 422–428.
[21] A.I. Bazhin, A.A. Goncharov, A.D. Pogrebnyak, V.A. Stupak, S.A. Goncharova, Superhardness effect in transition-metal diborides films, Phy. Met. Metallogr. 117 (2016) 594–601.
[22] V. Moraes, H. Riedl, C. Fuger, P. Polcik, H. Bolvardi, D. Holec, P.H. Mayrhofer, Ab initio inspired design of ternary boride thin films, Sci. Rep. 8 (2018) 9288.
[23] I. Matkovich, G.V. Samsonov, P. Hagenmuller, T. Lundstrom, Boron and Refractory Borides, First ed., Springer-Verlag, Berlin, Heidelberg, 1977.
[24] W.G. Fahrenholtz, G.E. Hilmas, I.G. Talmy, J.A. Zaykoski, Refractory diborides of zirconium and hafnium, J. Am. Ceram. Soc. 90 (2007) 1347–1364.
[25] M. Berger, M. Larsson, S. Hogmark, Evaluation of magnetron-sputtered TiB_2 intended for tribological applications, Surf. Coat. Technol. 124 (2000) 253–261.
[26] J.V. Rau, A. Latini, R. Teghil, A.D. Bonis, M. Fosca, R. Caminiti, V.R. Albertini, Superhard tungsten tetraboride films prepared by pulsed laser deposition method, ACS Appl. Mater. Interfaces 3 (2011) 3738–3743.
[27] F. Lofaj, T. Moskalewicz, G. Cempura, M. Mikula, J. Dusza, A. Czyrska-Filemonowicz, Nanohardness and tribological properties of nc-TiB_2 coatings, J. Eur. Ceram. Soc. 33 (2013) 2347–2353.
[28] A.T. Lech, C.L. Turner, J. Lei, R. Mohammadi, S.H. Tolbert, R.B. Kaner, Superhard rhenium/tungsten diboride solid solutions, J. Am. Chem. Soc. 138 (2016) 14398–14408.
[29] R.W. Cumberland, M.B. Weinberger, J.J. Gilman, S.M. Clark, S.H. Tolbert, R.B. Kaner, Osmium diboride, an ultra-incompressible, hard material, J. Am. Chem. Soc. 127 (2005) 7264–7265.
[30] H.Y. Chung, M.B. Weinberger, J.B. Levine, A. Kavner, J.M. Yang, S.H. Tolbert, R.B. Kaner, Synthesis of ultra-incompressible superhard rhenium diboride at ambient pressure, Science 316 (2007) 436–439.
[31] N. Nedfors, A. Mockute, J. Palisaitis, P.O.Å. Persson, L.Å. Näslund, J. Rosen, Influence of pulse frequency and bias on microstructure and mechanical properties of TiB_2 coatings deposited by high power impulse magnetron sputtering, Surf. Coat. Technol. 304 (2016) 203–210.
[32] J.B. Levine, S.H. Tolbert, R.B. Kaner, Advancements in the search for superhard ultra-incompressible metal borides, Adv. Funct. Mater. 19 (2009) 3519–3533.
[33] M.M. Zhong, X.Y. Kuang, Z.H. Wang, P. Shao, L.P. Ding, X.F. Huang, Phase stability, physical properties, and hardness of transition-metal diborides MB_2 (M = Tc, W, Re, and Os): first-principles investigations, J. Phys. Chem. C 117 (2013) 10643–10652.
[34] J. Lei, S. Hu, C.L. Turner, K. Zeng, M.T. Yeung, J. Yan, R.B. Kaner, S.H. Tolbert, Synthesis and high-pressure mechanical properties of superhard rhenium/tungsten diboride nanocrystals, ACS Nano 13 (2019) 0036–10048.
[35] A.S. Dranenko, V.A. Lavrenko, V.N. Talash, Corrosion resistance of nanostructured TiB_2 films in 3% NACl solution, Powder Metall. Met. Ceram. 49 (2010) 174–178.
[36] I.I. Korobov, G.V. Kalinnikov, A.V. Ivanov, N.N. Dremova, R.A. Andrievski, S.P. Shilkin, Corrosion resistance of nanostructured films of titanium diboride in mineral acid solutions, Prot. Met. Phys. Chem. Surf. 52 (2016) 618–621.

[37] A.D. McLeod, J.S. Haggetry, D.R. Sadoway, Electrical resistivities of monocrystalline and polycrystalline TiB_2, J. Am. Ceram. Soc. 67 (11) (1984) 705–708.
[38] M.V. Frandsen, W.S. Williams, Thermal conductivity and electrical resistivity of titanium diboride at low temperatures, J Hard Mater. 4 (1993) 113.
[39] Y. Wu, B. Messer, P. Yang, Superconducting MgB_2 nanowires, Adv. Mater. 13 (2001) 1487–1489.
[40] M. Bechelany, S. Bernard, A. Brioude, D. Cornu, P. Stadelmann, C. Charcosset, K. Fiaty, P. Miele, Synthesis of boron nitride nanotubes by a template-assisted polymer thermolysis process, J. Phys. Chem. C 111 (2007) 13378–13384.
[41] R. Arenal, O. Stephan, J.L. Cochon, A. Loiseau, Root-growth mechanism for single-walled boron nitride nanotubes in laser vaporization technique, J. Am. Chem. Soc. 129 (2007) 6183–16189.
[42] H. Gou, Z. Wang, J. Zhang, S. Yan, F. Gao, Structural stability and elastic and electronic properties of rhenium borides: first principle investigations, Inorg. Chem. 48 (2009) 581–587.
[43] X. Li, X. Yong, M. Wu, S. Lu, H. Liu, S. Meng, J.S. Tse, Y. Li, Hard BN clathrate superconductors, J. Phys. Chem. Lett. 10 (2019) 2554–2560.
[44] H. Zhang, Y. Li, J. Hou, A. Du, Z. Chen, Dirac state in the FeB_2 monolayer with graphene-like boron sheet, Nano Lett. 16 (2016) 6124–6129.
[45] T.T. Xu, J.G. Zheng, A.W. Nicholls, S. Stankovich, R.D. Piner, R.S. Ruoff, Single-crystal calcium hexaboride nanowires: synthesis and characterization, Nano Lett. 4 (2004) 2051–2055.
[46] V. Mazánek, H. Nahdi, J. Luxa, Z. Sofer, M. Pumera, Electrochemistry of layered metal diborides, Nanoscale 10 (2018) 11544–11552.
[47] Y. Jiang, Y. Lu, Designing transition-metal-boride-based electrocatalysts for applications in electrochemical water splitting, Nanoscale 12 (2020) 9327–9351.
[48] C. Lu, P.R. Jothi, T. Thersleff, T.M. Budnyak, A. Rokicinska, K. Yubuta, R. Dronskowski, P. Kuśtrowski, B.P.T. Fokwa, A. Slabon, Nanostructured core-shell metal borides–oxides as highly efficient electrocatalysts for photoelectrochemical water oxidation, Nanoscale 12 (2020) 3121–3128.
[49] D.P. Young, D. Hall, M.E. Torelli, Z. Fisk, J.L. Sarrao, J.D. Thompson, H.R. Ott, S.B. Oseroff, R.G. Goodrich, R. Zysler, High-temperature weak ferromagnetism in a low-density free-electron gas, Nature 397 (1999) 412–414.
[50] G. Akopov, M.T. Yeung, R.B. Kaner, Rediscovering the crystal chemistry of borides, Adv. Mater. 29 (2017) 1604506.
[51] H. Schmidt, G. Borchardt, S. Weber, H. Scherrer, Diffusion in transition metal diborides - an overview, Defect Diffus. Forum 263 (2007) 219–224.
[52] H. Schmidt, G. Borchardt, C. Schmalzried, R. Telle, S. Weber, H. Scherrer, Self-diffusion of boron in TiB_2, J. Appl. Phys. 93 (2003) 907–911.
[53] D. Lee, J.J. Vlassak, K. Zhao, First-principles theoretical studies and nanocalorimetry experiments on solid-state alloying of Zr-B, Nano Lett. 15 (2015) 6553–6558.
[54] J.E. Sundgren, B.O. Johansson, A. Rockett, S.A. Barnett, J.E. Greene, TiN: a review of the present understanding of the atomic and electronic structure and recent results on the growth and physical properties of epitaxial TiN_x ($0.6 < x < .12$) layers, in: W.D. Sproul, J.E. Greene, J.A. Thornton (Eds.), Physics and Chemistry of Protective Coatings, American Institute of Physics Series, vol. 149, 1986 New York.
[55] L.E. Toth, Transition Metal Carbides and Nitrides, First ed., Academic press, San Diego, CA, 1971.
[56] Facility for the Analysis of Chemical Thermodynamics. See: http://www.crct.polymtl.ca/fact/documentation/menu.php?SpMCBN=1.
[57] I. Petrov, A. Hall, A. Mei, N. Nedfors, I. Zhirkov, J. Rosén, A. Reed, B. Howe, G. Greczynski, J. Birch, L. Hultman, J.E. Greene, Controlling the boron-to-titanium ratio in magnetron-sputter-deposited TiB_x thin films, J. Vac. Sci. Technol. A 35 (2017) 050601.
[58] B. Bakhit, I. Petrov, J.E. Greene, L. Hultman, J. Rosen, G. Greczynski, Controlling the B/Ti ratio of TiB_x thin films grown by high-power impulse magnetron sputtering, J. Vac. Sci. Technol. A 36 (2018) 030604.
[59] W.J. Clegg, Controlling cracks in ceramics, Science 286 (1999) 1097.
[60] B. Bakhit, D.L.J. Engberg, J. Lu, J. Rosen, H. Högberg, L. Hultman, I. Petrov, J.E. Greene, G. Greczynski, Strategy for simultaneously increasing both hardness and toughness in ZrB_2-rich $Zr_{1-x}Ta_xB_y$ thin films, J. Vac. Sci. Technol. A 37 (2019) 031506.
[61] G. Greczynski, J. Lu, M.P. Johansson, J. Jensen, I. Petrov, J.E. Greene, L. Hultman, Role of Ti^{n+} and Al^{n+} ion irradiation ($n = 1, 2$) during $Ti_{1-x}Al_xN$ alloy film growth in a hybrid HIPIMS/magnetron mode, Surf. Coat. Technol. 206 (2012) 4202–4211.
[62] G. Greczynski, J. Lu, M. Johansson, J. Jensen, I. Petrov, J.E. Greene, L. Hultman, Selection of metal ion irradiation for controlling $Ti_{1-x}Al_xN$ alloy growth via hybrid HIPIMS/magnetron co-sputtering, Vacuum 86 (2012) 1036–1040.
[63] G. Greczynski, I. Petrov, J.E. Greene, L. Hultman, Paradigm shift in thin-film growth by magnetron sputtering: from gas-ion to metal-ion irradiation of the growing film, J. Vac. Sci. Technol. A 37 (2019) 060801.
[64] G. Greczynski, J. Lu, J. Jensen, I. Petrov, J.E. Greene, S. Bolz, W. Kölker, Ch. Schiffers, O. Lemmer, L. Hultman, Metal versus rare-gas ion irradiation during $Ti_{1-x}Al_xN$ film growth by hybrid high power pulsed magnetron/dc magnetron co-sputtering using synchronized pulsed substrate bias, J. Vac. Sci. Technol. A 30 (2012) 061504.
[65] G. Greczynski, J. Lu, S. Bolz, W. Kölker, C. Schiffers, O. Lemmer, I. Petrov, J.E. Greene, L. Hultman, Novel strategy for low-temperature, high-rate growth of dense, hard, and stress-free refractory ceramic thin films, J. Vac. Sci. Technol. A 32 (2014) 41515.
[66] W.H. Wang, C. Dong, C.H. Shek, Bulk metallic glasses, Mater. Sci. Eng. R 44 (2004) 45–89.
[67] J.P. Chu, J.S.C. Jang, J.C. Huang, H.S. Chou, Y. Yang, J.C. Ye, Y.C. Wang, J.W. Lee, F.X. Liu, P.K. Liaw, Y.C. Chen, C.M. Lee, C.L. Li, C. Rullyani, Thin film metallic glasses: unique properties and potential applications, Thin Solid Films 520 (2012) 5097–5122.
[68] D. Jang, J.R. Greer, Transition from a strong-yet-brittle to a stronger-and-ductile state by size reduction of metallic glasses, Nature Mater 9 (2010) 215–219.
[69] B. Post, F.W. Glaser, D. Moskowitz, Transition metal diborides Les biborures des métaux de transition Diboride der übergangsmetalle, Acta Metall. 2 (1954) 20.
[70] JCPDS International Centre for Diffraction Data. Zirconium diboride (ZrB_2) card 00-034-0423.
[71] JCPDS International Centre for Diffraction Data. Tantalum diboride (TaB_2) card 00-038-1462.
[72] M.J. Gasch, D.T. Ellerby, S.M. Johnson, Ultra high temperature ceramic composites, in: Narottam P. Bansal (Ed.), Handbook of Ceramic Composites, Springer Science & Business Media, New York, 2005.
[73] P. Vajeeston, P. Ravindran, C. Ravi, R. Asokamani, Electronic structure, bonding, and ground-state properties of AlB_2-type transition-metal diborides, Phys. Rev. B 63 (2001) 045115.
[74] M. Dahlqvist, U. Jansson, J. Rosen, Influence of boron vacancies on phase stability, bonding and structure of MB_2 (M=Ti, Zr, Hf, V, Nb, Ta, Cr, Mo, W) with AlB_2 type structure, J Phys. Condens. Matter 27 (2015) 435702.